CORPUS PUBLISHERS

Journal of Mineral and Material Science (JMMS)

ISSN: 2833-3616

Volume 7 Issue 1, 2026

Article Information

Received date : March 05, 2026

Published date: March 23, 2026

*Corresponding author

Freddy Humberto Escobar, Universidad Surcolombiana, Colombia

DOI: 10.54026/JMMS/1132

Key Words

Gas Hydrates; Thermodynamic; Hydrate-Bearing Region; Reservoir Dynamics

Research Article

Analytical Characterization of Gas Hydrate Reservoirs with Dynamic Dissociation Interfaces from Pressure and Rate Transient Tests

Miguel Renato Caicedo, Freddy Humberto Escobar* and Juan Pablo Salazar

Universidad Surcolombiana, Colombia

Abstract

Gas hydrate reservoirs represent a significant unconventional energy resource, but their production behavior is strongly influenced by hydrate dissociation processes that generate a moving interface between dissociated and intact zones. This dynamic boundary alters the transient pressure and rate responses of the reservoir, making conventional well-test interpretation methods difficult to apply.

In this work, an analytical methodology for the interpretation of transient pressure and rate tests in gas hydrate reservoirs is developed using the Tiab Direct Synthesis (TDS) technique. The formulation is based on a radial composite reservoir model with a dynamic dissociation interface proposed by Chen et al. [1]. By analyzing pseudo pressure, reciprocal rate, and their first- and second-order derivatives, characteristic points associated with hydrate dissociation dynamics are identified without the need for type-curve matching.

Using synthetic data generated from the analytical model, new explicit mathematical expressions were derived to estimate key reservoir parameters, including the dimensionless dissociation radius, the dissociation factor, and the interzonal storage ratio. The analysis demonstrates that the second-derivative functions provide clearer diagnostic features, such as local Minima and power-law slopes, which facilitate the identification of flow regimes and improve parameter estimation.

The proposed methodology successfully reproduces the dominant dynamics of hydrate reservoirs with moving dissociation fronts and provides reliable estimates of the governing parameters. These results demonstrate that the TDS-based framework offers a practical and fully analytical alternative for the interpretation of transient tests in hydrate-bearing formations.

Introduction

Gas hydrates are crystalline compounds formed by water and gas molecules, predominantly methane, that remain stable under conditions of high pressure and low temperature. These deposits are commonly found in marine sediments and permafrost environments and are considered one of the largest unconventional natural gas resources worldwide. The development of gas hydrate reservoirs, however, presents significant scientific and engineering challenges due to the complex coupling between multiphase flow, heat transfer, and phase-change processes associated with hydrate dissociation.

The conceptual foundations for modeling phase-change processes can be traced back to early thermodynamic studies. Black [2] introduced the concept of latent heat to describe melting and solidification phenomena, establishing the energetic basis for phase transitions. Later, Stefan [3] formalized the classical moving boundary problem describing the temporal evolution of phase interfaces through coupled energy balances. The Stefan problem has since become a fundamental theoretical framework for describing phase-change phenomena in porous media, including hydrate dissociation processes in subsurface formations. The thermodynamic conditions governing hydrate formation and stability were initially investigated in the mid-twentieth century. Carson & Katz [4] developed early practical correlations to predict hydrate formation conditions in natural gas mixtures, showing that hydrate formation behaves similarly to ideal solid solutions of gas components. Kobayashi & Katz [5] extended experimental measurements to higher pressures, while McLeod & Campbell [6] demonstrated that hydrate equilibrium at pressures between approximately 6,000 and 10,000 psi could be reasonably predicted using modified Clapeyron-type relationships. These early investigations established the thermodynamic basis for describing hydrate-gas-water equilibrium systems, consistent with the theoretical model later formalized by Van der Waals y Platteeuw [7].

Building upon these thermodynamic foundations, reservoir-scale models incorporating hydrate dissociation mechanisms have been developed over the past several decades [8] treated hydrate dissociation as a moving boundary problem, representing the advance of a dissociation front separating a region containing free gas from an outer region with intact hydrates. Tsypkin [9] subsequently developed a one-dimensional model describing coupled gas and water flow in hydrate-bearing formations, employing perturbation methods to obtain self-similar solutions for transient pressure and temperature behavior. More recently, Roostaie & Leonenko [10] proposed analytical models for vertical wells in hydrate reservoirs that explicitly consider the coexistence of dissociated and undissociated regions, as well as the influence of heat transport during gas production. Collectively, these studies established the composite reservoir framework with a moving dissociation front as a suitable representation of hydrate reservoir dynamics.

Analytical models describing well test responses in hydrate-bearing formations have continued to evolve. Chen et al. [1] proposed an analytical well test model that incorporates a dynamic dissociation interface and represents the reservoir as a two-region radial composite system. In this formulation, an inner dissociated region containing mobile gas and water expands over time within an outer region containing intact hydrates. By applying the Laplace transform and numerical inversion using the Stehfest algorithm, Stehfest [11] these authors obtained a semi-analytical solution for bottom-hole pressure and identified transient flow regimes associated with the propagation of the dissociation front.

In parallel, numerical simulation tools capable of coupling thermal, chemical, and multiphase flow processes have been developed to model hydrate production. For example, Moridis et al. [12] introduced the TOUGH+Hydrate simulator, which solves coupled mass, energy, and geomechanical balance equations to represent hydrate dissociation in multilayer reservoirs. Such simulators provide detailed representations of hydrate systems but often require significant computational resources and extensive parameter calibration.

Experimental investigations have also contributed substantially to the understanding of hydrate behavior in porous media. Holder et al. [13] examined the thermal aspects of hydrate dissociation by solving conjugate heat transfer equations coupled with gas continuity equations. Subsequent studies highlighted that heat stored within sediments can locally accelerate hydrate dissociation, while the generation of free gas and water alters relative permeabilities and flow pathways. Laboratory-scale experiments using microfluidic models have provided additional insight into pore-scale dissociation mechanisms. For instance, Li et al. [14] visualized hydrate dissociation fronts in glass micromodels and observed that thick water films surrounding hydrates can hinder gas diffusion, creating a front-blocking effect that slows dissociation. At larger scales, imaging techniques such as Magnetic Resonance Imaging (MRI) and Computed Tomography (CT) have been used to characterize phase distributions during hydrate dissociation. Waite et al. [15] demonstrated that hydrate distribution and pore-scale morphology strongly influence the effective permeability and mechanical response of hydrate-bearing sediments. Similarly, Kou et al. [16] showed that different gas occurrence patterns lead to distinct hydrate morphologies, which in turn affect pore connectivity and flow mechanisms during formation and dissociation processes.

The analysis of well tests in hydrate reservoirs presents additional challenges due to the dynamic nature of hydrate dissociation and the resulting evolution of reservoir properties. Kome et al. [17] developed analytical well test models for Class 3 hydrate reservoirs characterized by a single hydrate-bearing layer without initially mobile gas or water. Their results demonstrated that the presence of a dynamic dissociation interface significantly alters the transient pressure response and may distort interpretations based on classical constant-rate assumptions developed for conventional reservoirs. More recently, Ma et al. [18] developed a transient rate analysis model for multilateral horizontal wells incorporating moving boundaries representing dissociating hydrate zones, while Chu et al. [19] proposed a meshless analytical approach for multilateral wells that divides the reservoir into dissociated and intact hydrate regions.

Within the context of well test interpretation, methodologies that allow the direct identification of flow regimes without relying exclusively on type-curve matching have gained increasing attention. Early developments in this direction were introduced by Tiab y Kumar [20], who applied analytical pressure functions to interference test analysis. Tiab [21,22] later formalized the Tiab Direct Synthesis (TDS) technique, which uses characteristic points of pressure and pressure-derivative curves to estimate reservoir parameters without dependence on type-curve matching procedures. The TDS technique has since been successfully applied to increasingly complex reservoir systems. For example, Tiab y Bettam [23] applied direct synthesis methods to pressure tests in naturally fractured reservoirs with hydraulically fractured wells, while Molina et al. [24] used the method to estimate average reservoir pressure in naturally fractured formations. Escobar et al. [25] extended the TDS framework to transient rate analysis in gas reservoirs, and subsequent studies demonstrated its applicability to fractured horizontal wells and heterogeneous systems [26,27].

Despite these advances, the interpretation of transient pressure and rate responses in hydrate reservoirs remains challenging due to the evolving hydraulic properties associated with hydrate dissociation and the presence of composite regions with contrasting flow characteristics. These complexities motivate the development of interpretation methodologies capable of extracting reservoir information without relying exclusively on numerical simulation or type-curve matching procedures. In this context, the application of the TDS technique to hydrate-bearing reservoirs provides a promising analytical framework for linking diagnostic features observed in pressure and pressure-derivative responses with characteristic reservoir parameters. Analytical expressions derived under this framework allow the direct estimation of quantities associated with the dissociation process, including the effective radius of the dissociated zone, the dissociation factor, and the storage relationship between altered and intact regions, using information obtained from transient well tests [28].

Mathematical Model

In this work, the model proposed by Chen et al. [1] is adopted as the basis for describing gas hydrate reservoirs with a dynamic dissociation interface. The model describes transient radial flow of a slightly compressible single-phase fluid in a porous medium with an infinite boundary, assuming uniform initial pressure and flow governed by Darcy's law. In addition, gravitational and capillary forces are considered negligible. Wellbore storage and formation damage effects are included, with production occurring at a constant rate in a formation of uniform thickness. The system is represented by two radial zones (Figure 1) with different mobility and storage properties, characterized by the ratios M_{12} and ω_{12}. Hydrate dissociation is modeled through a dynamic interface with a dissociation radius R*, which varies with time as a function of the dissociation factor λ and the diffusivity of the inner zone η_1, which is assumed constant to facilitate the development of the model.

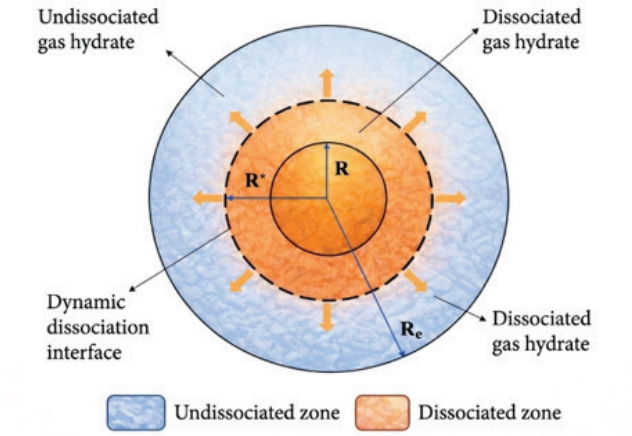

Figure 1: Gas hydrate reservoir with a dynamic dissociation interface. The solid line represents the outer undissociated zone, and the dashed line represents the inner dissociated zone, [28].

The diffusivity equations in radial coordinates for the inner and outer zones are defined as follows:

$$\frac{\partial^2 m(P)_1}{\partial r^2} + \frac{1}{r}\frac{\partial m(P)_1}{\partial r} = \frac{1}{3.6\eta_1}\frac{\partial m(P)_1}{\partial t} \quad (1)$$

$$\frac{\partial^2 m(P)_2}{\partial r^2} + \frac{1}{r}\frac{\partial m(P)_2}{\partial r} = \frac{1}{3.6\eta_2}\frac{\partial m(P)_2}{\partial t} \quad (2)$$

The internal boundary condition is given by:

$$\left(\frac{\partial m(P)_w}{\partial r}\right)_{r=rw} = \frac{3.684\times10^{-3} q\mu_1 B_{tl}}{k_1 h} \quad (3)$$

Other boundary conditions:

$$m(P)_2(r\to\infty, t) = m(P)_1 \quad (4)$$

$$m(P)_1(r,0) = m(P)_2(r,0) = m(P)_i \quad (5)$$

$$m(P)_1(R^*,t) = m(P)_2(R^*,t) \quad (6)$$

The dimensionless variables are introduced below:

$$r_D = \frac{r}{r_w} \quad (7)$$

$$C_D = \frac{c}{2\pi\phi c_t h r_w^2} \quad (8)$$

$$m(P_D) = \frac{k_1 h(\Delta m(P))}{3.684\times10^{-3}\mu_1^2 B_H q_{sc}} \quad (9)$$

$$t_D = \frac{3.6 k_1 t}{\mu_1 \phi c_t r_w^2} \quad (10)$$

Based on the variables introduced above, the following expressions were obtained from Equations (1) and (2):

$$\frac{\partial^2 m(P_D)_1}{\partial r_D^2} + \frac{1}{r_D}\frac{\partial m(P_D)_1}{\partial r_D} = \frac{\partial m(P_D)_1}{\partial t_D} \quad (11)$$

$$\frac{\partial^2 m(P_D)_2}{\partial r_D^2} + \frac{1}{r_D}\frac{\partial m(P_D)_2}{\partial r_D} = X_{12}\frac{\partial m(P_D)_2}{\partial t_D} \quad (12)$$

The internal boundary condition, in dimensionless form, is expressed as:

$$\left(r_D \frac{\partial m(P_D)_1}{\partial r_D}\right)_{r_D=1} = -1 \quad (13)$$

The dimensionless inner boundary condition is expressed as:

$$m(P_D)_2(r \to \infty, t_D) = 0 \quad (14)$$

The initial conditions and the interface boundary condition in dimensionless form are expressed as:

$$m(P_D)_1(r_D, 0) = m(P_D)_2(r_D, 0) = 0 \quad (15)$$

$$m(P_D)_1(R^*, t_D) = m(P_D)_2(R^*, t_D) \quad (16)$$

The model was solved in the Laplace domain, providing the pressure drop in the inner and outer zones.

$$m(\bar{P}_D)_1(r_D, u) = \frac{\left[v\left[K_1(\sqrt{u})I_0(r_D\sqrt{u}) + K_0(r_D\sqrt{u})I_1(\sqrt{u})\right] - \frac{1}{u^{1.5}}\left[KI\cdot K_0(r_D\sqrt{u}) + I_0(r_D\sqrt{u})\right]\right]}{I_1(\sqrt{u}) - KI\cdot K_1(r_D\sqrt{u})} \quad (17)$$

$$m(\bar{P}_D)_2(r_D, u) = \frac{K_0(r_D\sqrt{X_{12}u})}{K_0(b)} \frac{v\left[I_0(a)K_1(\sqrt{u}) + K_0(a)I_1(\sqrt{u})\right] - \frac{1}{u^{1.5}}\left[KI\cdot K_0(a) + I_0(a)\right]}{\left[I_1(\sqrt{u}) - KI\cdot K_1(\sqrt{u})\right]} \quad (18)$$

Where:

$$KI = \frac{K_0(b)I_1(a) + \frac{1}{M_{12}}\sqrt{X_{12}}I_0(a)K_1(b)}{K_0(b)K_1(a) - \frac{1}{M_{12}}\sqrt{X_{12}}K_0(a)K_1(b)} \quad (19)$$

$$V = \frac{\lambda_D' = K_0(b)}{\frac{u}{M_{12}}\sqrt{X_{12}}K_0(a)K_1(b) - u\cdot K_0(b)K_1(a)} \quad (20)$$

$$\lambda_D' = 2\sqrt{\pi} Z T \phi S_H B_H \gamma_w \frac{\pi h}{B q_{sc}} \frac{P_{sc}}{T_{sc}} \sqrt{\frac{3.6 K_1}{\mu_1 \phi c_t r_w^2}} \sqrt{\eta_1 \lambda} \quad (21)$$

By applying the principle of superposition, the solution for the pressure drop at the well, including skin and wellbore storage effects, is given by:

$$m(\bar{P}_D)_w = \frac{u\cdot m(\bar{P})(u) + S}{u\{1 + C_D u[m(\bar{P})(u) + S]\}} \quad (22)$$

Where $m(\bar{P})w$ is the flowing bottomhole pseudo pressure in the Laplace domain excluding skin and wellbore storage effects, I_0, I_1, K_0, and K_1 are modified Bessel functions, and u is the complex Laplace transform variable.

TDS Framework

For the development of the present work, the following definitions, from previous works, were considered:

$$t_D = \left(\frac{0.0002637kt}{\phi\mu c_t r_w^2}\right) \quad (23)$$

$$t_{Da} = \left(\frac{0.0002637kt_a}{\phi r_w^2}\right) \quad (24)$$

$$(m(P_D')) = \left(\frac{0.000703kh(\Delta m(P'))}{q_{sc}T}\right) \quad (25)$$

$$t_{Da} * m(P_D') = \left(\frac{0.000703kh(t_a * m(\Delta P'))}{q_{sc}T}\right) \quad (26)$$

$$(t_{Da}^2 * m(P_D'')) = \left(\frac{0.000703kh(t_a^2 * \Delta m(P''))}{q_{sc}T}\right) \quad (27)$$

$$1/q_D' = \left(\frac{0.000703kh(1/q)}{P_{wf}T}\right) \quad (28)$$

$$(t_{Da} * (1/q_D')) = \left(\frac{0.000703kh(t_a * (1/q'))}{P_{wf}T}\right) \quad (29)$$

$$(t_{Da}^2 * (1/q_D'')) = \left(\frac{0.000703kh(t_a^2 * (1/q''))}{P_{wf}T}\right) \quad (30)$$

$$k = \frac{711.26qT}{h[t_a * \Delta m(P'))]_r} \quad (31)$$

$$k = \frac{711.26 P_{wf} T}{h[t_a * 1/q')]_r} \quad (32)$$

Using the mathematical model proposed by Chen et al. [1], several simulations were conducted to analyze the behavior of a gas hydrate reservoir. In these simulations, model parameters such as λ and R_i were varied to evaluate the sensitivity of the system. Subsequently, the responses obtained allowed the identification of characteristic points and, through curve normalization, the formulation of mathematical expressions based on the TDS technique. The analysis considered pressure as well as its first- and second-order derivative functions under conditions of constant flowing bottomhole pressure and constant flow rate.

Pressure Transient Analysis

Figure 2 illustrates the effect of the inner radius R_i, which directly influences the evolution of the flow regimes. As R_i decreases, the transition associated with the dynamic interface occurs at earlier times, reducing the duration of the radial flow regime within the inner zone. Conversely, larger values of R_i extend this regime and shift the characteristic response toward later dimensionless times.

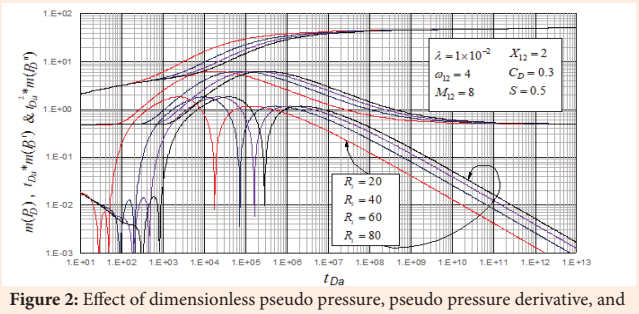

Figure 2: Effect of dimensionless pseudo pressure, pseudo pressure derivative, and second pseudo pressure derivative for different values of R_i.

Following the adjustment-which is shown in Figure 3-and upon scaling the time axis, a characteristic point was identified in the (t_{Da}*m(P_D')) curves, corresponding to a local maximum. To facilitate its identification and interpretation, the decision was made to work with the (t_{Da}^2*m(P_D")) representation, in which this feature manifests as a more clearly defined local minimum.

Subsequently, through a temporal normalization process, the results of which are shown in Figure 3, it was observed that scaling the time allows the identification of a characteristic point in the $t_{Da}{}^{2}*m(P_D'')$ curves corresponding to a local maximum. In order to facilitate its identification and improve graphical interpretation, the representation $t_{Da}{}^{2}*m(P_D'')$ was adopted, where this feature appears as a more clearly defined local minimum.

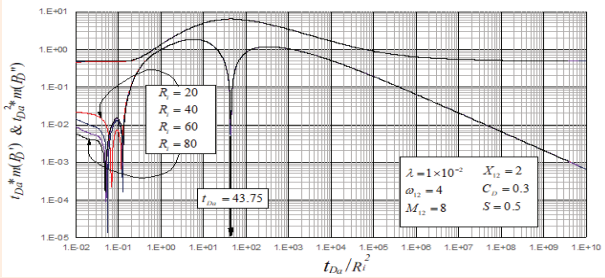

Figure 3: Unified behavior of the dimensionless pseudo pressure derivative, and second pseudo pressure derivative for different values of R_i.

From this minimum, Equation (33) was obtained.

$$\frac{t_{Da}}{R_i^2} = 43.75 \quad (33)$$

By substituting Equation (24) into Equation (33), Equation (34) was obtained.

$$\frac{\left(\frac{0.0002637 k_i (t_a)_{min_{(t_a^2 * m(\Delta P''))}}}{\phi r_w^2}\right)}{R_i^2} = 43.75 \quad (34)$$

Solving for R_i yields the following expression, which is valid for calculating the radius of the dissociated hydrate zone:

$$R_i = \frac{2.5\times10^{-3}}{r_w}\sqrt{\frac{k(t_a)_{min_{(t_a^2 * m(\Delta P''))}}}{\phi}} \quad (35)$$

Figure 4 shows that the dissociation factor (λ) controls the rate at which the dissociation front propagates through the porous medium. This parameter modifies the temporal position of the flow regimes dominated by gas contribution from the hydrate-bearing zone. As λ increases, the response associated with the moving interface occurs at earlier times and the decline observed in the derivative function during the dissociation stage becomes more pronounced. Conversely, lower values of λ attenuate this effect and shift its manifestation toward later dimensionless times.

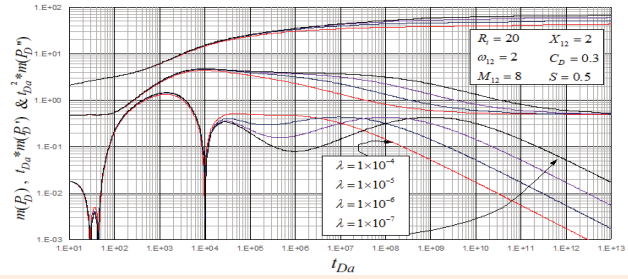

Figure 4: Effect of dimensionless pseudo pressure, pseudo pressure derivative, and second pseudo pressure derivative for different values of λ.

Subsequently, through the temporal normalization process shown in Figure 5, it was observed that after rescaling the time the curves of $t_{Da}{}^{2}*m(P_D'')$ exhibit a power-law behavior with a slope similar to that associated with the spherical flow regime. Based on this region, a power-law regression was performed on the slope of $t_{Da}{}^{2}*m(P_D'')$, from which an analytical expression valid for calculating the dissociation factor λ was obtained. In this context, the identified slope constitutes the characteristic feature directly used in the formulation of the proposed interpretation method.

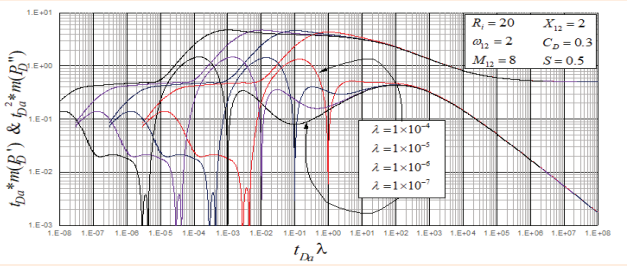

Figure 5: Unified behavior of the pseudo pressure derivative and second pseudo pressure derivative for different values of λ.

The general power-law equation is given by:

$$y = bx^m \quad (36)$$

Where: $y = t_{Da}{}^{2}*m(P_D'')$, $b = 16.1$, $x = t_{Da}\lambda$, $m = -0.495$

By substituting the previous values into Equation (36), the following expression was obtained:

$$0.5 = 16.1(t_{Da}\lambda)^{-0.495} \quad (37)$$

By substituting Equation (24) into Equation (37), and considering that the value of $t_{Da}*m(P_D')$ during radial flow is 0.5, Equation (38) was obtained.

$$0.5 = 16.1\left(\frac{0.0002637 k t_{a(r-r'')_i}}{\phi r_w^2}\lambda^1\right)^{-0.495} \quad (38)$$

Solving for λ yields the following expression, which is valid for calculating the hydrate dissociation factor:

$$\lambda = 4.25\times10^{6}\left(\frac{\phi r_w^2}{k t_{a(r-r'')_i}}\right) \quad (39)$$

Figure 6 shows that the storage ratio (ω_{12}) directly influences the magnitude of the transient response associated with the transition regime between the inner and outer zones. As ω_{12} increases, the characteristic local maximum observed in the $t_{Da}*m(P_D')$ curves becomes more pronounced, indicating a stronger contrast in storage capacity between both regions and a more significant transient exchange between them. Conversely, for lower values of ω_{12}, the amplitude of this hump decreases, reflecting a smoother system response and a reduced influence of differential storage on pressure dynamics.

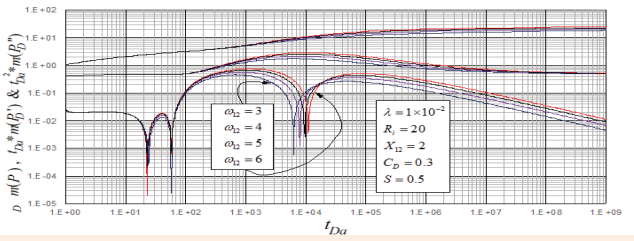

Figure 6: Effect of the dimensionless pseudo pressure derivative and second pseudo pressure derivative for different values of ω_{12}.

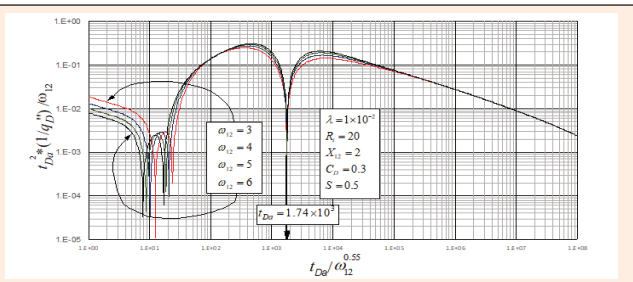

Figure 7: Unified behavior of the dimensionless pseudo pressure derivative and second pseudo pressure derivative for different values of ω_{12}.

Subsequently, through the normalization process shown in Figure 7, after rescaling the variables t_{Da} and $t_{Da}{}^{2*}m(P_D'')$, an interval was identified in which the curves exhibit a power-law behavior. Within this region, a power-law regression was performed on the slope observed in $t_{Da}{}^{2*}m(P_D'')$, following a procedure analogous to that applied previously.

Accordingly, a power-law regression was defined as, where: $y = (t_{Da}{}^{2*}m(P_D''))/(\omega_{12})^{0.9}$, b = 33.047, $x = t_{Da}/(\omega_{12})^{0.81}$, m = -0.495, These values were then substituted into Equation (36), yielding the following expression:

$$\left(\frac{t_{Da}^2 * m\left(\Delta P_D''\right)}{\omega_{12}^{0.9}}\right) = 33.047\left(\frac{t_{Da}}{\omega_{12}^{0.81}}\right)^{-0.497} \quad (40)$$

Substituting Equations (24) and (27) into Equation (40) yielded Equation (41).

$$\left(\frac{\left(\frac{0.000703kh(t_a^2 * \Delta m(P''))_{r''}}{q_{sc}T}\right)}{\omega_{12}^{0.9}}\right) = 33.047\left(\frac{\left(\frac{0.0002637kt_{a(r'')}}{\phi r_w^2}\right)}{\omega_{12}^{0.81}}\right)^{-0.497} \quad (41)$$

Solving for ω_{12} yields the following explicit expression for calculating the storage ratio, using the slope directly as the characteristic point of the interpretation method.

$$\omega_{12} = 1.062 \times 10^{-5}\left(\frac{kh(t_a^2 * \Delta m(P''))_{r''}}{q_{sc}T}\left(\frac{kt_{a(r'')}}{\phi r_w^2}\right)^{0.497}\right)^{0.77} \quad (42)$$

Synthetic Example 1

Figure (8) presents the synthetic pressure test obtained from the simulator developed in this study. The input parameters used in the simulation are detailed below:

q = 353.1 MSCF r_w = 0.814 ft T = 545.7 R ϕ = 0.415 μ = 0.016 cp
c_t = 6.21x10^{-7} psi^{-1} h = 65.62 ft

From Figure (8), the following characteristic points were selected:

ta(r") =6.80x10^8 psi hr/cp
$t_a{}^{2*}\Delta m(P'')_r$ = 1.09x10^4 psi^2/cp
$t_{a(r''-r'')i}$ = 3.1 x10^7 psi hr/cp
$t_a{}^{2*}\Delta m(P')_r$ = 4.77x10^4 psi^2/cp
$t_{a(min}(t_a{}^{2*}{}_{\Delta m(P'')}))$ = 1.81x10^5 psi hr/cp

Initially, permeability was calculated using Equation (31).

$$k = \frac{711.26(353.1)(545.7)}{(65.62)(4.77 \times 10^4)} = 43.828md$$

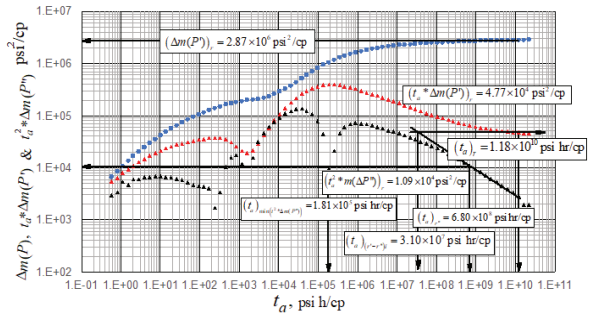

Figure 8: Log-log plot of pseudo pressure, pseudo pressure derivative, and second pseudo pressure derivative versus pseudo time for synthetic example 1.

Subsequently, the values of key dimensionless parameters -such as the dissociation radius, dissociation factor, and storage ratio- were obtained using Equations (35), (39), and (42).

$$R_i = \frac{2.5 \times 10^{-3}}{(0.814)}\sqrt{\frac{(43.828)(1.81\times 10^5)}{(0.415)}} = 13.43$$

$$\lambda = 4.25 \times 10^6\left(\frac{(0.415)(0.814)}{(43.828)(3.1 \times 10^7)}\right) = 1 \times 10^{-3}$$

$$\omega_{12} = 1.062 \times 10^{-5}\left(\left(\frac{(43.828)(65.62)(1.09 \times 10^4)}{(353.1)(545.7)}\right)\left(\frac{(43.828)(6.80 \times 10^8)}{(0.415)(0.814)^2}\right)^{0.497}\right)^{0.77} = 8.3$$

Results are reported and compared in table 1.

Table 1: Comparison of results for synthetic example 1.

Parameter	Input Data	This Study
R_i	20	13.2
λ	1x10^{-3}	1x10^{-3}
ω_{12}	8	8.3

Transient Rate Analysis

In transient rate analysis, a behavior analogous to that previously described for transient pressure is observed, where the dissociation factor λ controls the dynamics of the moving interface and the transition between flow regimes dominated by gas contribution from the hydrate-bearing zone. This behavior is illustrated in Figure (9).

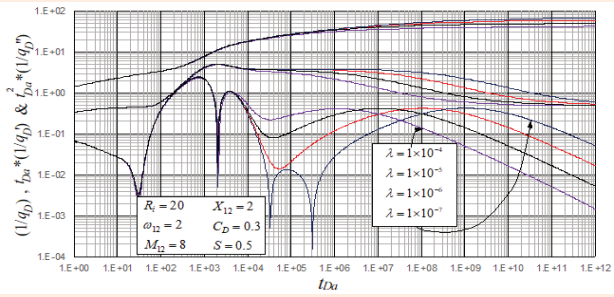

Figure 9: Effect of the dimensionless reciprocal rate, the derivative of the reciprocal rate, and the second derivative of the reciprocal rate for different values of λ.

Subsequently, a rescaling procedure of the dimensionless variables was performed, as shown in Figure (10). In the curves of $t_{Da}{}^{2*}m(1/q_D'')$, a characteristic maximum point was identified that remains clearly defined for different values of the dissociation factor λ. Based on this characteristic point, an analytical expression was derived to estimate the hydrate dissociation factor λ.

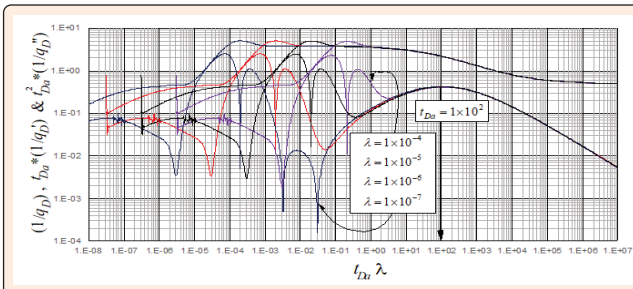

Figure 10: Unified behavior of the dimensionless reciprocal rate, the derivative of the reciprocal rate, and the second derivative of the reciprocal rate for different values of λ.

Using the value of the maximum point identified in the second-order derivative function, Equation (43) was obtained.

$$t_{Da}\lambda = 100 \quad (43)$$

Equation (24) was substituted into Equation (43), resulting in Equation (44).

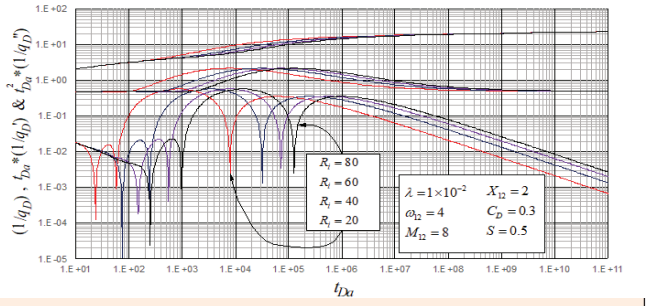

Figure 11: Effect of the dimensionless reciprocal rate, the derivative of the reciprocal rate, and the second derivative of the reciprocal rate for different values of R_i.

Finally, solving for λ yielded the expression shown below:

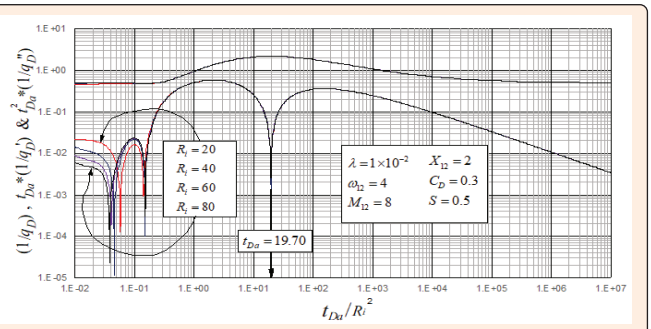

Figure 12: Unified behavior of the dimensionless derivative of the reciprocal rate and the second derivative of the reciprocal rate for different values of R_i.

$$\left(\frac{0.0002637kt}{\phi r_w^2\, a\left(hump\left(t_{ia}^2*\left(\frac{1}{q''}\right)\right)\right)}\right)\lambda = 100 \quad (44)$$

Finally, solving for λ yielded the expression shown below:

$$\lambda = 3.791\times10^5\left(\frac{\phi r_w^2}{kt\, a\left(hump\left(t_{ia}^2*\left(\frac{1}{q''}\right)\right)\right)}\right) \quad (45)$$

Figure (11) presents the effect of the inner radius R_i on the log-log representation of the reciprocal rate and its first- and second derivative functions. Since the influence of R_i was previously analyzed in the context of pressure behavior, the analysis under rate conditions shows equivalent trends, which are mainly reflected in the temporal shift of the characteristic response.

The observed behavior and the matching procedure used for the analysis of the reciprocal rate and its derivative functions are shown in Figure (12). The obtained results exhibit behavior consistent with that previously observed in the pressure analysis.

From this minimum point, Equation (46) was obtained.

$$\frac{t_{Da}}{R_i^2} = 19.70 \quad (46)$$

Equation (24) was substituted into Equation (46), yielding Equation (47).

$$\frac{\left(\frac{0.0002637kt}{\phi r_w^2\, a\left(min\left(t_{ia}^2*\left(\frac{1}{q''}\right)\right)\right)}\right)}{R_i^2} = 19.70 \quad (47)$$

Solving for R_i yields the following expression, which is valid for calculating the radius of the dissociated hydrate zone:

$$R_i = \frac{3.7\times10^{-3}}{r_w}\sqrt{\frac{kt}{\phi\, a\left(min\left(t_{ia}^2*\left(\frac{1}{q''}\right)\right)\right)}} \quad (48)$$

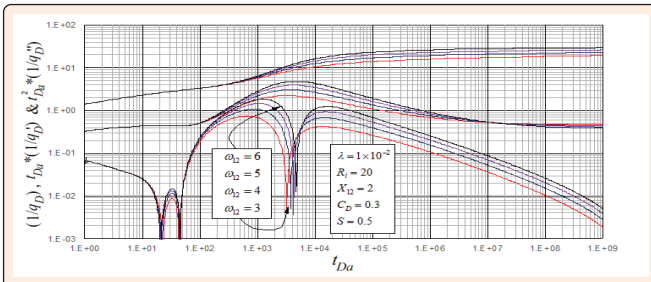

Figure 13: Effect of the dimensionless reciprocal rate, the derivative of the reciprocal rate, and the second derivative of the reciprocal rate for different values of ω_{12}.

Figure (13) shows that the storage ratio (ω_{12}) influences the transient response in a manner similar to that previously observed in the transient pressure analysis. In this case, the minimum point of the derivative function was selected as the characteristic point for interpreting the system behavior.

The rescaling procedure used to obtain the unified behavior of the curves around this minimum point is shown in Figure (14).

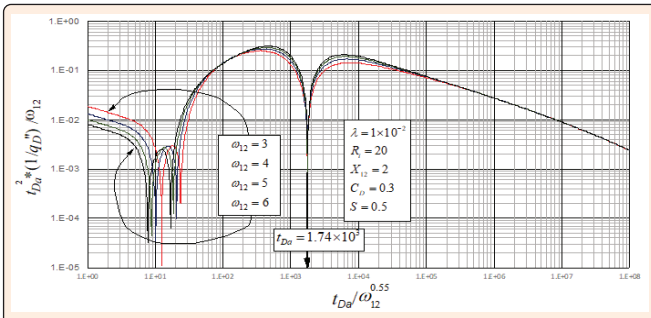

Figure 14: Unified behavior of the dimensionless derivative of the reciprocal rate and the second derivative of the reciprocal rate for different values of ω_{12}.

From the value of this minimum point, Equation (49) was obtained.

$$\frac{t_{Da}}{\omega_{12}^{0.55}} = 1.74\times10^3 \quad (49)$$

By substituting Equation (24) into Equation (49), Equation (50) was derived.

$$\frac{\left(\frac{0.0002637kt}{\phi r_w^2\, a\left(min\left(t_{ia}^2*\left(\frac{1}{q''}\right)\right)\right)}\right)}{\omega_{12}^{0.55}} = 1.74\times10^3 \quad (50)$$

Solving for ω_{12} yields the expression used to calculate the storage ratio between the dissociated and the undissociated zones.

$$\omega_{12} = 4\times10^{-13}\left(\frac{kt}{\phi r_w^2\, a\left(min\left(t_{ia}^2*\left(\frac{1}{q''}\right)\right)\right)}\right)^{1.82} \quad (51)$$

Synthetic Example 2

Figure 15 presents the synthetic rate test generated using the simulator developed in this study. The input parameters used in the simulation are listed below.

P_{wf} = 3500 psi r_w = 0.814 ft T = 545.7 R ϕ = 0.415

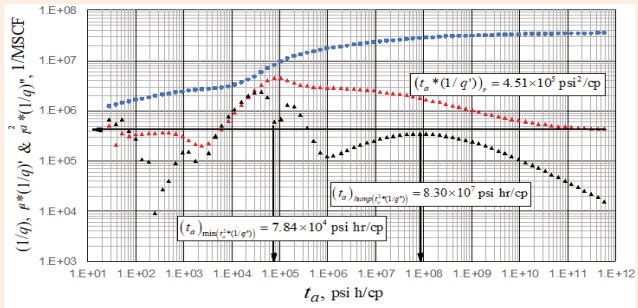

Figure 15: Log-log plot of reciprocal rate, reciprocal rate derivative and second reciprocal rate derivative for synthetic example 2.

μ = 0.016 cp $c_t = 9\text{x}10^{-7}$ psi^{-1} h = 65.62 ft

From Figure 15, the following characteristic points were selected:

$t_{a(hump(ta^2*(1/q')))}$=8.30x10^7 psi hr/cp $(t_a*(1/q'))_r$ = 4.51x10^5 psi^2/cp

$t_{a(min(ta^2*(1/q')))}$ = 7.84x10^4 psi hr/cp

First, permeability was calculated using Equation (31).

$$k = \frac{711.26(3500)(545.7)}{(65.62)(4.51\times10^5)} = 45.9md$$

Subsequently, the values of key dimensionless parameters -such as the dissociation radius, the dissociation factor, and the storage ratio-were obtained using Equations (45), (48), and (51). The results are summarized in Table 2.

$$\lambda = 3.791\times10^5\left(\frac{(0.415)(0.814)^2}{(45.9)(8.30\times10^7)}\right) = 2.7\times10^5$$

$$\omega_{12} = 4\times10^{-13}\left(\frac{(45.9)(7.84\times10^4)}{(0.415)(0.814)^2}\right)^{1.82} = 3.6$$

$$R_i = \frac{3.7\times10^{-3}}{(0.814)}\sqrt{\frac{(45.9)(7.84\times10^4)}{(0.415)}} = 13.4$$

Table 2: Comparison of results for synthetic example 2.

Parameter	Input Data	This Study
R_i	28	13.4
λ	5x10^{-5}	2.7x10^{-5}
ω_{12}	4	3.6

Comments on the Results

The dimensionless parameters obtained for synthetic example 1 (R_i=13.43, λ =0.001 and ω_{12}=8.3) indicate the presence of a well-developed dissociation interface, characterized by slow dissociation kinetics and a strong storage contrast between zones. The low value of the dissociation factor λ reflects a gradual propagation of the dissociation front, which delays the gas contribution from the hydrate-bearing region. At the same time, the relatively high storage ratio ω_{12} promotes a pronounced transitional regime, associated with the exchange of mass between the dissociated and undissociated regions. Consequently, the transient pressure response reproduces the characteristic behavior of hydrate reservoirs with a mobile dissociation interface, consistent with the physical assumptions of the base model.

In contrast, synthetic example 2, analyzed under transient rate conditions, exhibits a markedly different dynamic. The high dissociation factor λ =270000 indicates a rapid advance of the dissociation front, which causes the reservoir to behave similarly to a nearly homogeneous system dominated by the dissociated region. The value R_i=13.4 confirms the presence of a widely propagated dissociation front, while the moderate storage ratio ω_{12}=3.6 suggests a moderate contrast in storage capacity between the two zones. Under these conditions, the response of the reciprocal rate and its first- and second-order derivatives reflects a system mainly governed by fast dissociation kinetics, rather than by prolonged transitional effects.

A comparison between the input parameters of the simulator and those estimated using the TDS technique reveals a good level of consistency for both pressure and rate analyses, although some differences are observed. For the pressure-transient case, the dissociation factor λ is reproduced exactly, while the storage ratio ω_{12}shows excellent agreement (8 vs 8.3), confirming the reliability of the method in estimating the storage contrast between zones. However, the dimensionless radius Ri is underestimated (20 vs 13.2), suggesting that the TDS formulation tends to slightly compress the radial extension of the dissociation front. The sensitivity of the reading may cause the difference.

A similar trend is observed in the reciprocal rate analysis, where the dissociation radius is again underestimated (28 vs 13.4). The dissociation factor λ preserves the correct order of magnitude with only minor deviations from the simulator input value, while the storage ratio ω_{12}exhibits a satisfactory agreement (4 vs 3.6). Overall, the proposed TDS methodology successfully captures the dominant dynamics of the system and the characteristic magnitude of the governing parameters, although it shows a systematic tendency to smooth the spatial development of the moving dissociation interface.

Conclusion

This study presents an analytical methodology for the interpretation of transient pressure and rate tests in gas hydrate reservoirs with a dynamic dissociation interface. The formulation is based on the two-zone radial composite model proposed by Chen et al. [1], which adequately represents the physical behavior of hydrate dissociation processes in porous media. The selected mathematical framework allows the interaction between the dissociated and undissociated regions to be described explicitly, capturing the transient dynamics associated with the dissociation radius and the evolving reservoir response. From this theoretical basis, pressure, reciprocal rate, and their first- and second-order derivatives were generated and analyzed to evaluate the influence of the most representative parameters governing hydrate dissociation.

The derivative-based analysis enables the identification of characteristic points associated with distinct flow regimes and the transition between reservoir zones. Using these characteristic features, explicit analytical expressions were derived following the Tiab Direct Synthesis (TDS) methodology, eliminating the need for type-curve matching and strengthening the analytical nature of the interpretation procedure. This approach enables the direct estimation of key parameters such as the dissociation factor λ and the interzonal storage ratio (ω_{12}).

Application of the methodology to synthetic cases demonstrates good agreement with the reference physical model, confirming the capability of the proposed technique to characterize hydrate reservoirs with moving dissociation fronts. Although a slight bias was observed in the estimation of the dissociation radius R_i, the overall accuracy of the parameter estimation remains satisfactory.

Overall, the proposed methodology provides a robust and practical analytical tool for the interpretation of transient tests in gas hydrate reservoirs, offering a direct alternative for the characterization of dissociation dynamics in this class of unconventional resources.

Acknowledgment

The authors would like to express sincere gratitude to Dr. Zhiming Chen from the State Key Laboratory of Oil and Gas Reservoir Geology and Exploitation, Chengdu University of Technology, China, for his valuable assistance in the programming and implementation of the mathematical model used in this work. His technical insight and support were instrumental in resolving a critical issue encountered during the development of the computational solution, which ultimately enabled the successful application of the analytical methodology presented in this study.

References

1. Chen Z, Li D, Zhang S, Liao X, Zhou B, et al. (2022) A well-test model for gas hydrate dissociation considering a dynamic interface. Fuel 314: 123053.
2. Black J (1803) Lectures on the elements of chemistry: Delivered in the University of edinburgh, Mundell and Son.
3. Stefan J (1891) On the theory of ice formation, particularly on ice formation in the polar ocean. Annalen der Physik 278(2): 269-286.
4. Carson DB, Katz DL (1942) Natural gas hydrates. Transactions of the AIME 146(01): 150-158.
5. Kobayashi R, Katz DL (1949) Methane hydrate at high pressure. Journal of Petroleum Technology 1(03): 66-70.
6. McLeod HO, Campbell JM (1961) Natural gas hydrates at pressures to 10,000 psia. Journal of Petroleum Technology 13(06): 590-594.
7. Waals JHVD, Platteeuw JC (1958) Clathrate Solutions. En I Prigogine (Ed.) Advances in Chemical Physics Wiley 2: 1-57.
8. Makogon YF (1981) Hydrates of Natural Gas (1st edn) PennWell Publishing Company.
9. Tsypkin GG (1993) Mathematical model of the dissociation of gas hydrates coexisting with ice in natural reservoirs. Fluid Dynamics 28(2): 223-229.
10. Roostaie M, Leonenko Y (2020) Gas production from methane hydrates upon thermal stimulation; an analytical study employing radial coordinates. Energy 194: 116815.
11. Stehfest H (1970) Algorithm 368: Numerical inversion of Laplace transforms [D5]. Communications of the ACM 13(1): 47-49.
12. Moridis GJ, Kowalsky MB, Karsten (2008) TOUGH+HYDRATE v1.0 user's manual: A code for the simulation of system behavior in hydrate-bearing geologic media. Lawrence Berkeley National Laboratory.
13. Holder George D, Katz David L, Hand JH (1976) Hydrate formation in subsurface environments. AAPG Bulletin 60:6.
14. Li M, Fan S, Su Y, Xu F, Li Y, et al. (2018) The Stefan moving boundary models for the heat-dissociation hydrate with a density difference. Energy 160: 1124-1132.
15. Waite WF, Santamarina JC, Cortes DD, Dugan B, Espinoza DN, et al. (2009) Physical properties of hydrate-bearing sediments. Reviews of Geophysics 47(4): 2008RG000279.
16. Kou X, Li XS, Wang Y, Liu JW, Chen ZY (2021) Effects of gas occurrence pattern on distribution and morphology characteristics of gas hydrates in porous media. Energy 226: 120401.
17. Kome M, Amro M, Cinar Y (2013) Analytical models for well test analysis in class 3 gas hydrate reservoirs. SPE Reservoir Characterization and Simulation Conference and Exhibition SPE-165975-MS.
18. Ma T, Chu H, Li J, Zhang J, Gao Y et al. (2024) Rate transient analysis for multilateral horizontal well in natural gas hydrate: Superposition principle and reciprocity. International Journal of Coal Science & Technology 11(1): 70.
19. Chu H, Zhang J, Zhu W, Kong D, Ma T, et al. (2023) A quick and reliable production prediction approach for multilateral wells in natural gas hydrate: Methodology and case study. Energy 277: 127667.
20. Tiab D, Kumar A (1980) Application of the p'D function to interference analysis. Journal of Petroleum Technology 32(08): 1465-1470.
21. Tiab D (1993) Analysis of pressure and pressure derivative without type-curve matching-iii vertically fractured wells in closed systems. SPE Western Regional Meeting SPE-26138-MS.
22. Tiab D (1995) Analysis of pressure and pressure derivative without type-curve matching-skin and wellbore storage. Journal of Petroleum Science and Engineering 12(3): 171-181.
23. Tiab D, Bettam Y (2007) Practical interpretation of pressure tests of hydraulically fractured wells in a naturally fractured reservoir. Latin American and Caribbean Petroleum Engineering Conference SPE-107013-MS.
24. Molina M, Escobar FH, Monte Alegre MM, Restrepo DP (2005) Application of the TDS technique for determining the average reservoir pressure for vertical wells in naturally fractured reservoirs. CT&F - Ciencia, Tecnología y Futuro 3(1): 45-55.
25. Escobar F, Sánchez JA, Cantillo JH (2008) Rate transient analysis for homogeneous and heterogeneous gas reservoirs using the TDS technique. CT&F - Ciencia, Tecnología y Futuro, 3(4): 45-59.
26. Escobar FH, Rojas JD, Ghisays-Ruiz A (2015) Rate transient analysis for hydraulically-fractured horizontal wells in naturally-fractured shale gas reservoirs 10(1).
27. Escobar FH, Jongkittnarukorn K, Hernandez CM (2019) The power of TDS technique for well test interpretation: A short review. Journal of Petroleum Exploration and Production Technology 9(1): 731-752.
28. Google (2024) Gemini [Software] Google LLC.

Nomenclature

M_{12}	Mobility ratio between inner and outer zone.
X_{12}	Diffusivity ratio between inner and outer zone.
R_i	Dimensionless radius of the dissociated zone.
c_t	Compressibility factor, psi^{-1}
T	Temperature, R
C	Wellbore storage coefficient, bbl/psi
c_t	Total system compressibility
k	Permeability of zone 1, md
K_0	Modified Bessel function of the second kind (order zero)
K_1	Modified Bessel function of the second kind (order one)
I_0	Modified Bessel function of the first kind (order zero)
I_0	Modified Bessel function of the first kind (order one)
h	Reservoir thickness, ft
P_{wf}	Flowing bottom hole pressure, psi
q	Flow rate, MSCF
r_w	Wellbore radius, ft
u	Complex variable of the Laplace transform
S	Skin
t_a	Pseudotime, psi·hr/cp
$\Delta m(P')$	Pseudopressure, psi^2/cp
$ta^* \Delta m(P')$	Derivative function of pseudopressure, psi^2/cp
$t_{Da}{}^{2*} \Delta m(P'')$	Second derivative function of pseudopressure, psi^2/cp
1/q	Reciprocal of flow rate, 1/MSCF
$t_a*(1/q')$	Derivative function of the reciprocal flow rate, 1/MSCF
$t_{Da}{}^{2*}(1/q'')$	Second derivative function of the reciprocal flow rate, 1/MSCF

Greek

λ	Dissociation factor
ω_{12}	Storage ratio between inner and outer zone
ϕ	Porosity of zone 1
μ	Viscosity, cp

Subscripts

min	Minimum
hump	Maximum
D	Dimensionless
r	Radial flow
r''	Radial flow observed in the second derivative function
i	Intercep